# Spacecraft Attitude Determination Using Recursive Discrete-Time Estimation Techniques

Holly Dinkel, Andrew Gatherer, Kevin Tracy, Jayden Zundel

Stanford University, AA273 Spring 2019 Final Project

**Abstract**

Fast and efficient inter-satellite communications represents a growing need in the satellite industry as optical communications enables forwarding of data to other satellites which can immediately downlink this data to ground stations. State estimation is important for successful inter-satellite communication: the state of a spacecraft must be determined with high accuracy for successful pointing, acquisition, and tracking before data can be transferred between satellites. The importance of filtering is further underlined when a satellite operates with limited star tracker ability. In this project, we build a dynamics simulation based on the evolution of the spacecraft's state, comprising its angular velocity and quaternion with noise, over time. The dynamics simulation includes measurement of the state over time with measurement noise. The Extended Kalman Filter (EKF), Multiplicative Extended Kalman Filter (MEKF), and the Unscented Kalman Filter (UKF) were implemented, and the Root-Mean-Squared (RMS) error between each filter estimate and the true state was tracked and compared between the three filters for a spacecraft with three different rotation rates. The performance of the three filters was compared based on RMS error and computation time.

# Introduction

The number of satellites in orbit continues to increase exponentially with the advent of small satellites and large mega-constellations. The burgeoning of this industry has prompted a need for fast and efficient inter-satellite communications. Rather than store information onboard until the next opportunity for ground-station downlink, satellites enabled by optical communication can transmit data immediately to other satellites, which can forward important data to ground users. Satellite mega-constellations like the SpaceX Starlink constellation can only achieve feasibility through efficient inter-satellite links. This agility is required to minimize latency for communication satellite constellations. Optical communication offers the only viable communication method since the bit rate and signal issues inherent to radio frequency (RF) communication is amplified at such long distances. In eliminating bulky and power-hungry RF components, optical communication systems also offer reductions in Size, Weight, and Power (SWaP) for small satellites.

A nascent area of research interest is optimization of Pointing, Acquisition, and Tracking (PAT) accuracy, as precise attitude measurement and control are required for sustained free-space optical communication. Additionally, Low-Earth Orbit (LEO) satellite constellations complicated control and communication link due to smaller orbital periods. Satellites must execute fast maneuvers and achieve communication before geometry precludes communication due to distance or horizon issues. When performing communication, LEO satellites must both predict and control their attitude effectively and efficiently.

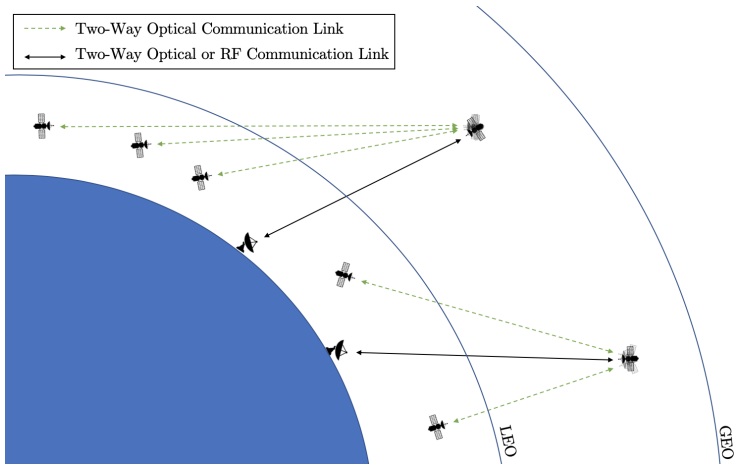


Figure 1: Optical satellite communication network where all data to and from LEO satellites are routed through a GEO satellite for constant communication with a ground station.

Compared against LEO-to-Geostationary Orbit (GEO) links depicted in Figure 1, optical links between satellites in LEO require additional PAT accuracy, as both the target and the emitter are travelling at significant velocities. Attitude estimation poses a significant limitation to technological readiness, as the sensor noise of both the emitting satellite and target satellite affect the combined optical communication. For small satellites with star trackers, the accuracy of this attitude measurement tool precludes the need for advanced filters that model the non-linear behaviour of the system. If satellites operate with faulty or limited star trackers, the importance of the filtering mechanism increases significantly. The exponentially-increasing computational ability of satellites enables use of more advanced filters for better state estimation.

# Related Work

## State Estimation Techniques

The intersection of Kalman filters and spacecraft state estimation has grown since the inception of spaceflight. The modified Multiplicative EKF (MEKF) first proposed by Lefferts et al. [7] allowed for the expression of a global representation of spacecraft attitude with a minimum number of parameters and without running into singularity issues. The unit quaternions proposed appear linearly in the kinematic equations of motion whereas the Euler angles conventionally used to describe kinematics require expensive computation of trigonometric functions. The MEKF is also appealing because the covariance matrix of the four elements in the quaternion does not require computation, which offers a substantial increase in computational efficiency over Kalman filter implementations. The drawback of the MEKF, that all three-dimensional Euler angle representations are singular or discontinuous for certain attitudes, was addressed by Filipe et al. [4] which proposed a Dual Quaternion MEKF (DQ-MEKF); where $\mathbf{q}_r$ is the real part of the quaternion, $\mathbf{q}_d$ is the dual part, and $\epsilon$ is the dual unit, the dual quaternion $\mathbf{q}$ is $\mathbf{q} = \mathbf{q}_r + \epsilon\mathbf{q}_d$. When written in terms of dual quaternions, the estimation of the combined translational and rotational dynamics take the same form as the rotational-only dynamics; the DQ-MEKF enables estimation of both attitude (Euler angles) and position.

The use of dual quaternions has also been implemented in the Unscented Kalman Filter (UKF), originally developed to avoid the errors caused by linearization in the EKF ([6],[11]). The UKF is difficult

to implement with quaternion logic due to the normalization constraint of quaternions, but this problem has been overcome by Deng et al. [2] through the use of twistors, a mathematical property which represent the relative pose in terms of dual quaternions. The twistor-based UKF was shown to outperform the DQ-MEKF in cases of highly nonlinear behavior or significant initial attitude errors.

Faruqi and Turner [3] explored the application of EKFs to improve navigation accuracy with Global Positioning System (GPS)/Inertial Navigation System (INS) sensors for aviation. For optical communication between satellites in LEO, GPS can be used to improve the high-level accuracy of satellite PAT. Compared to GEO-GEO and GEO-LEO optical communications, LEO-LEO geometry changes very rapidly, as the satellites quickly pass each other and move past the horizon. In light of this dynamic environment, the position of the satellites gives insight into the change in relative position and attitude required to maintain an optical link. By including position and velocity in the state and integrating an EKF-based GPS measurement into the filter, overall computational efficiency improved.

In surveying nonlinear attitude control methods, Crassidis and Cheng [1] recognized the longevity of the application of the MEKF to satellite systems, surpassing newer and more complex filters. The MEKF is limited at points of significant nonlinear dynamics, presence of significant sensor noise, or when initial state estimate is poor. For these situations, the UKF is preferred as it provides accurate filtering at slightly more computational expense. The Particle Filter and the Quanternion Estimation algorithm are generally outperformed by the MEKF, UKF, and EKF in satellite attitude estimation.

### Optical Communications

Intersatellite links were first demonstrated with the European Space Agency's SILEX mission [9], demonstrating the possibility of transferring significant amounts of data from LEO to GEO. The SILEX mission results indicated that satellite vibrations and optical sensor noise posed a risk to the success optical communications missions [10]. The SILEX mission also demonstrated the importance of the acquisition method and maintenance procedure given a known required attitude accuracy for minimizing optical loss. The Optical Communicator and Sensor Demonstration project aims to bring optical communications to small satellites with a $0.065^o$ pointing accuracy for laser operation [5] and was validated successfully on-orbit.

## Dynamics

This project considers torque-free attitude dynamics for spacecraft simulation. The comparative filter strengths are validated outside of any form of control through momentum wheels, gas jets, or other attitude maneuvering methods. The two primary reference frames considered are the normal and body reference frames. The normal, or inertial, frame represents a static frame in space. As the satellite moves around its orbit, the x-axis of the normal frame stays fixed in the direction of the point of Ares during the Vernal Equinox and the z-axis is perpendicular to the orbital plane of the Earth. The body frame is fixed with respect to the satellite, such that any fixture of the spacecraft maintains a set body frame coordinate for the entirety of the simulation; the rotation between inertial space and the spacecraft is modeled as a rotation between the inertial frame and the body frame. Figure 2 displays the normal and body reference frames.

Spacecraft motion can be viewed from the perspective of angular momentum, defined as $\mathbf{L} = \mathbf{r} \times \mathbf{p}$ where $\mathbf{r}$ and $\mathbf{p}$ are the position and momentum vectors of the object in question. For any satellite rotating around its center of mass, the dynamics are dictated by the sum of the angular momentum of the equivalent particles in the satellite. The change in angular momentum in the rotating reference frame is related

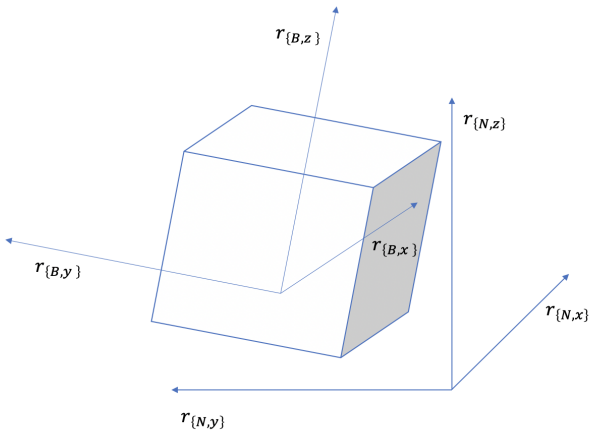


Figure 2: Spacecraft reference frames

to the input moments given by the torques acting on the body and the current rotation rate of the vehicle, as seen in Equation (1). The rotation rate of the vehicle in Equation (1), $\boldsymbol{\omega}$, is the vector of rotation rate of the vehicle around each of its three principal axes as shown in Equation (2).

$$\left(\frac{d\mathbf{L}}{dt}\right)_{rot} + \boldsymbol{\omega} \times \mathbf{L} = \sum \boldsymbol{\tau} \tag{1}$$

$$\boldsymbol{\omega} = \begin{bmatrix} \omega_x \\ \omega_y \\ \omega_z \end{bmatrix} \tag{2}$$

If the principle moments and tensors of inertia can be assumed to be constant for the spacecraft, then $\mathbf{L} = \boldsymbol{I}\boldsymbol{\omega}$ where $\boldsymbol{I}$ is the inertia tensor. Euler's rigid body dynamics equations can be seen in Equation (3).

$$\boldsymbol{I}\dot{\boldsymbol{\omega}} + \boldsymbol{\omega} \times (\boldsymbol{I}\boldsymbol{\omega}) = \sum \boldsymbol{\tau} \tag{3}$$

Equation (3) can be rearranged to solve for the angular accelerations given no external torques shown in Equation (4).

$$\dot{\boldsymbol{\omega}} = \boldsymbol{I}^{-1}[-\boldsymbol{\omega} \times (\boldsymbol{I}\boldsymbol{\omega})] \tag{4}$$

Euler's equations of motion exhibit strong non-linear tendencies, so any linearization of a state vector containing rotation rate must ignore some portion of the true dynamics. The dynamics are often linearized assuming small rotation rates, as is discussed in the EKF implementation. This work uses quaternions to avoid the singularities seen with Euler angles or other linearized parameterizations of spacecraft attitude. Quaternions are non-singular representations of a given rotation, similar to a rotation matrix. However, quaternions are represented by a three-component vector component and a single-component scalar, while rotation matrices comprise nine-component scalars; quaternions are more computationally efficient. Equation (5) gives a quaternion in terms of the axis of rotation, $\mathbf{e}$, and the rotation amount, $\theta$.

$$\mathbf{q} = \begin{bmatrix} \hat{\mathbf{e}}_x \sin(\theta/2) \\ \hat{\mathbf{e}}_y \sin(\theta/2) \\ \hat{\mathbf{e}}_z \sin(\theta/2) \\ \cos(\theta/2) \end{bmatrix} \tag{5}$$

The time derivative of the quaternion is expressed as Equation (6), where $\Omega$ is the skew symmetric matrix shown in Equation (7).

$$\dot{\mathbf{q}} = \frac{1}{2}\Omega\mathbf{q} \tag{6}$$

$$\Omega = \begin{bmatrix} 0 & \omega_z & -\omega_y & \omega_x \\ -\omega_z & 0 & \omega_x & \omega_y \\ \omega_y & -\omega_x & 0 & \omega_z \\ -\omega_x & -\omega_y & -\omega_z & 0 \end{bmatrix} \tag{7}$$

## Inertia Tensor

Another consideration for spacecraft dynamics is the inertia tensor. An inertia tensor that is diagonal only has moments of inertia about the three body axes, and has zero products of inertia between the axes. When the inertia tensor is diagonal, linearization of Euler's rigid body equations is simple. However, almost no spacecraft are able to achieve a perfectly diagonal inertia tensor, such as ours in Equation (8).

$$\mathbf{I}^{SC/SC_0} = \begin{bmatrix} 208.6262 & -11.57 & -11.57 \\ -11.57 & 275.44 & -5.6 \\ -11.57 & -5.6 & 213.65 \end{bmatrix} kg \cdot m^2 \tag{8}$$

While the products of inertia are low, they are not zero and the inertia tensor is not diagonal. This means that in the spacecraft body axes, the inertia tensor is not diagonal. However, for every spacecraft there exists a set of principal axes such that the inertia tensor is diagonal. To find the principal axes and the inertia tensor expressed in principal axes, the eigenvalues of the body axes inertia tensor must be determined as shown in Equations (9, 10).

$$|\mathbf{I}^{SC/SC_0} - \boldsymbol{\lambda}\mathbf{I}| = 0 \tag{9}$$

$$\left| \begin{bmatrix} 208.6262 & -11.57 & -11.57 \\ -11.57 & 275.44 & -5.6 \\ -11.57 & -5.6 & 213.65 \end{bmatrix} - \boldsymbol{\lambda} \begin{bmatrix} 1 & 0 & 0 \\ 0 & 1 & 0 \\ 0 & 0 & 1 \end{bmatrix} \right| = 0 \tag{10}$$

The eigenvalue solution to Equation (10) is shown in Equation (11) and the eigenvectors determined from these eigenvalues are shown in Equation (12).

$$\lambda_1 = 197.284\,;\ \lambda_2 = 222.835\,;\ \lambda_3 = 277.601 \tag{11}$$

$$\mathbf{V}_1 = \begin{bmatrix} 0.7798 \\ 0.1588 \\ 0.6056 \end{bmatrix}\ ;\ \mathbf{V}_2 = \begin{bmatrix} -0.6064 \\ -0.0489 \\ 0.7936 \end{bmatrix}\ ;\ \mathbf{V}_3 = \begin{bmatrix} -0.1556 \\ 0.9861 \\ -0.0582 \end{bmatrix} \tag{12}$$

The eigenvectors from Equation (12) can be used to generate the rotation matrix, ${}^P\mathbf{R}^B$, from the body axes to the principal axes as shown in Equation (13).

$${}^P\mathbf{R}^B = \begin{bmatrix} 0.7798 & -0.6064 & -0.1556 \\ 0.1588 & -0.0489 & 0.9861 \\ 0.6056 & 0.7936 & -0.0582 \end{bmatrix} \tag{13}$$

The rotation matrix ${}^{P}\mathbf{R}^{B}$ is used to convert body centered axis to principal axis locations to diagonalize the inertia tensor from Equation (8). The resulting inertia tensor about these principal axes is shown in Equation (14).

$$\mathbf{I}^{SC/SC_0}_{principal} = \begin{bmatrix} 197.2836 & 0 & 0 \\ 0 & 222.835 & 0 \\ 0 & 0 & 277.60 \end{bmatrix} kg \cdot m^2 \tag{14}$$

This process can be repeated for the diagonalization of any non-diagonal inertia tensor. This simulation and state estimation use the inertia tensor about the principal axes, from here on represented simply as $\mathbf{I}$ for convenience. With the inertia tensor diagonalized, the components of the angular acceleration can be expressed as Equation (15).

$$\dot{\omega}_x = \frac{(I_y - I_z)w_y w_z}{I_x} \; ; \; \dot{\omega}_y = \frac{(I_z - I_x)w_z w_x}{I_y} \; ; \; \dot{\omega}_z = \frac{(I_x - I_y)w_y w_x}{I_z} \tag{15}$$

## Simulation Structure

Because spacecraft motion is highly nonlinear, even a low $\delta t$ will produce significant divergence from the true solution if simple Euler integration is used. The simulation used in this project addresses this problem by using a variable-time-step ordinary differential equation (ODE) solver with solutions propagated at intervals of $\delta t$. This allows for highest possible numerical accuracy while adding the flexibility of adding process noise and sampling at fixed time steps. The dynamics simulation comprises the ODE solver and the simulation script shown in the following solver blocks.

### ODE Solver

**Function** $[\dot{\boldsymbol{\omega}}, \dot{\mathbf{q}}]$ = **ODE**($\boldsymbol{\omega}$, $\mathbf{q}$,$\mathbf{I}$)

$$\dot{\boldsymbol{\omega}} = \mathbf{I}^{-1}[-\boldsymbol{\omega} \times (\mathbf{I}\boldsymbol{\omega})] \qquad \text{Angular velocities}$$

$$\Omega = \begin{bmatrix} 0 & \omega_z & -\omega_y & \omega_x \\ -\omega_z & 0 & \omega_x & \omega_y \\ \omega_y & -\omega_x & 0 & \omega_z \\ -\omega_x & -\omega_y & -\omega_z & 0 \end{bmatrix}$$

$$\dot{\mathbf{q}} = \frac{1}{2}\Omega\mathbf{q} \qquad \text{Quaternion kinematics}$$

**end**

**Simulation Script**

simulation time = 100 seconds
sampling rate = 100 Hz
$\delta t$ = 0.001 seconds

**for** i = 1 : (simulation time · sampling rate)

$$\begin{aligned}
\mathbf{Q}_{noise} &= \text{mvnrnd}(\mathbf{0}, \mathbf{Q}) \\
\mathbf{R}_{noise} &= \text{mvnrnd}(\mathbf{0}, \mathbf{R}) \\
[\boldsymbol{\omega}_{t=i\cdot\delta t}, \mathbf{q}_{t=i\cdot\delta t}] &= \textbf{ODEsolver}(\boldsymbol{\omega}_{t=(i-1)\cdot\delta t}, \mathbf{q}_{t=(i-1)\cdot\delta t}, \textbf{ODE}, \delta t) + \mathbf{Q}_{noise} \\
\mathbf{y}_{t=(i-1)\cdot\delta t} &= \begin{bmatrix} \boldsymbol{\omega} \\ \mathbf{q} \end{bmatrix}_{t=(i-1)\cdot\delta t} + \mathbf{R}_{noise}
\end{aligned}$$

**end**

The simulation inputs are initial attitude and angular velocity, and the simulation is run for a given sampling rate and total simulation time. Process and measurement noises were re-sampled and added to process and measurement dynamics, respectively, at every time step.

# Methodology

We plan to implement an Extended Kalman Filter (EKF), a quaternion Multiplicative Extended Kalman Filter (MEKF) and a modified Unscented Kalman Filter (UKF) to estimate the attitude of simulated spacecraft subjected to inputs of solar radiation pressure, magnetic field, torques due to drag, and the gravity gradient. To quantify filter performance, we will track the estimation error over time. We will vary the relative velocities of the satellites, significantly affecting the PAT requirements of the system. For satellites that are moving quickly, the nonlinear dynamics are expected to become more pronounced, and we expect the error between the UKF estimate and the true state to be smaller than the error estimate of the EKF and the true state and the MEKF and the true state. Additionally, magnitude of sensor noise affects the performance of the filter. We plan to model limited star tracker ability by increasing sensor noise and compare the performance of the EKF, MEKF, and the UKF by determining the Root-Mean-Squared (RMS) error for each filter.

## Extended Kalman Filter

The Kalman Filter (KF) is a Bayesian filter applicable to linear systems, in the form of Equations (16, 17).

**Predict Step (KF)**

$$\begin{aligned}
\boldsymbol{\mu}_{t|t-1} &= \mathbf{A}_t\boldsymbol{\mu}_{t-1|t-1} + \mathbf{B}_t\mathbf{u}_t \\
\boldsymbol{\Sigma}_{t|t-1} &= \mathbf{A}_t\boldsymbol{\Sigma}_{t-1|t-1}\mathbf{A}_t^T + \mathbf{Q}
\end{aligned} \tag{16}$$

**Update Step (KF)**

$$\begin{aligned}
\mathbf{K}_t &= \boldsymbol{\Sigma}_{t|t-1}\mathbf{C}_t^T\mathbf{C}_t^T[\mathbf{C}_t\boldsymbol{\Sigma}_{t|t-1}\mathbf{C}_t^T + \mathbf{R}_t]^{-1} \\
\boldsymbol{\mu}_{t|t} &= \boldsymbol{\mu}_{t|t-1} + \mathbf{K}_t[\mathbf{y}_t - \mathbf{C}_t\boldsymbol{\mu}_{t|t-1}] \\
\boldsymbol{\Sigma}_{t|t} &= \boldsymbol{\Sigma}_{t|t-1} - \mathbf{K}_t\mathbf{C}_t\boldsymbol{\Sigma}_{t|t-1}
\end{aligned} \tag{17}$$

The KF requires the system dynamics be described in a linear form as in Equation (18).

$$\dot{\mathbf{x}} = \mathbf{A}\mathbf{x} + \mathbf{B}\mathbf{u} \tag{18}$$

The dynamics of a spinning spacecraft cannot be linearized as in Equation (18), therefore the KF cannot adequately determine the spacecraft state. The EKF was developed for state estimation of systems with dynamical and measurement models that could be approximated by a linear model. The dynamical model and measurement model are represented as Equation (19).

$$\begin{aligned} \mathbf{x}_{t+1} &= f(\mathbf{x}_t, \mathbf{u}_t) \\ \mathbf{y}_t &= g(\mathbf{x}_t) \end{aligned} \tag{19}$$

The measurement function is full state feedback, and the dynamics function can be discretized according to Equation (20).

$$\begin{aligned} w_{t+1}^x &= w_t^x + \delta t \tfrac{(I_y - I_z) w_t^y w_t^z}{I_x} \\ w_{t+1}^y &= w_t^y + \delta t \tfrac{(I_z - I_x) w_t^z w_t^x}{I_y} \\ w_{t+1}^z &= w_t^z + \delta t \tfrac{(I_x - I_y) w_t^x w_t^y}{I_z} \\ q_{t+1}^1 &= q_t^1 + \tfrac{1}{2}\delta t(w_t^x q_t^4 - w_t^y q_t^3 + w_t^z q_t^2) \\ q_{t+1}^2 &= q_t^2 + \tfrac{1}{2}\delta t(w_t^x q_t^3 + w_t^y q_t^4 - w_t^z q_t^1) \\ q_{t+1}^3 &= q_t^3 + \tfrac{1}{2}\delta t(w_t^y q_t^1 - w_t^x q_t^2 + w_t^z q_t^4) \\ q_{t+1}^4 &= q_t^4 + \tfrac{1}{2}\delta t(-w_t^x q_t^1 - w_t^y q_t^2 - w_t^z q_t^3) \end{aligned} \tag{20}$$

Equation (20) comprises the discrete-time dynamic model $f$ where the state $\mathbf{x}$ is represented by Equation (21).

$$\mathbf{x} = \begin{bmatrix} \omega_x & \omega_y & \omega_z & q_1 & q_2 & q_3 & q_4 \end{bmatrix}^T \tag{21}$$

The EKF predict and update steps are furthermore represented as Equations (22, 23), with $\mathbf{A}_t$ and $\mathbf{C}_t$ further defined in Equations (24–27).

**Predict Step (EKF)**

$$\begin{aligned} \boldsymbol{\mu}_{t|t-1} &= f(\boldsymbol{\mu}_{t-1|t-1}, \mathbf{u}_t) \\ \boldsymbol{\Sigma}_{t|t-1} &= \mathbf{A}_t \boldsymbol{\Sigma}_{t-1|t-1} \mathbf{A}_t^T + \mathbf{Q}_t \end{aligned} \tag{22}$$

**Update Step (EKF)**

$$\begin{aligned} \mathbf{K}_t &= \boldsymbol{\Sigma}_{t|t-1} \mathbf{C}_t^T \mathbf{C}_t^T [\mathbf{C}_t \boldsymbol{\Sigma}_{t|t-1} \mathbf{C}_t^T + \mathbf{R}_t]^{-1} \\ \boldsymbol{\mu}_{t|t} &= \boldsymbol{\mu}_{t|t-1} + \mathbf{K}_t [\mathbf{y}_t - g(\boldsymbol{\mu}_{t|t-1})] \\ \boldsymbol{\Sigma}_{t|t} &= \boldsymbol{\Sigma}_{t|t-1} - \mathbf{K}_t \mathbf{C}_t \boldsymbol{\Sigma}_{t|t-1} \end{aligned} \tag{23}$$

The jacobian of the dynamical model, $\mathbf{A}_t$, is used to convert the system dynamics from continuous and nonlinear to discrete and linear, as shown in Equations (24, 25).

$$\mathbf{A}_t = \left[\frac{\partial f}{\mathbf{x}_t}\right] \tag{24}$$

$$\mathbf{A}_t = \begin{bmatrix} 1 & \delta t\frac{(I_y-I_z)w_t^z}{I_x} & \delta t\frac{(I_y-I_z)w_t^y}{I_x} & 0 & 0 & 0 & 0 \\ \delta t\frac{(I_z-I_x)w_t^z}{I_y} & 1 & \delta t\frac{(I_z-I_x)w_t^x}{I_y} & 0 & 0 & 0 & 0 \\ \delta t\frac{(I_x-I_y)w_t^y}{I_z} & \delta t\frac{(I_x-I_y)w_t^x}{I_z} & 1 & 0 & 0 & 0 & 0 \\ \frac{1}{2}\delta t q_t^4 & -\frac{1}{2}\delta t q_t^3 & \frac{1}{2}\delta t q_t^2 & 1 & \frac{1}{2}\delta t w_t^z & -\frac{1}{2}\delta t w_t^y & \frac{1}{2}\delta t w_t^x \\ \frac{1}{2}\delta t q_t^3 & \frac{1}{2}\delta t q_t^4 & -\frac{1}{2}\delta t q_t^1 & -\frac{1}{2}\delta t w_t^z & 1 & \frac{1}{2}\delta t w_t^x & \frac{1}{2}\delta t w_t^y \\ -\frac{1}{2}\delta t q_t^2 & \frac{1}{2}\delta t q_t^1 & \frac{1}{2}\delta t q_t^4 & \frac{1}{2}\delta t w_t^y & -\frac{1}{2}\delta t w_t^x & 1 & \frac{1}{2}\delta t w_t^z \\ -\frac{1}{2}\delta t q_t^1 & -\frac{1}{2}\delta t q_t^2 & -\frac{1}{2}\delta t q_t^3 & -\frac{1}{2}\delta t w_t^3 & -\frac{1}{2}\delta t w_t^y & -\frac{1}{2}\delta t w_t^z & 1 \end{bmatrix} \tag{25}$$

The measurement jacobian, $\mathbf{C}_t$, is used to discretize and linearize the measurement model, as shown in Equations (26, 27).

$$\mathbf{C}_t = \left[\frac{\partial g}{\mathbf{x}_t}\right] \tag{26}$$

$$\mathbf{C}_t = \mathbf{I}_{7\times 7} \tag{27}$$

## Multiplicative Extended Kalman Filter

The MEKF [7] represents the attitude as the quaternion product $\mathbf{q}_k$ with parameters $\mathbf{q}_{ref}$, a reference quaternion, and the rotation $\delta\mathbf{q}(\mathbf{a})$. Where $\boldsymbol{\omega}_k$ is the rotation rate of the satellite, the state vector is represented by Equation (28).

$$\mathbf{x}_k = \begin{bmatrix} \boldsymbol{\omega}_k \\ \mathbf{q}_k \end{bmatrix} \tag{28}$$

The state is initially propagated through the traditional nonlinear dynamics equations. The forward dynamics are dictated by $\theta = ||\boldsymbol{\omega}_k||\delta t$ and $\boldsymbol{r} = \frac{\boldsymbol{\omega}_k}{||\boldsymbol{\omega}_k||}$. In these relations, $\theta_k$ represents the difference in angle between time steps, $\mathbf{r}_k$ is the rotation vector about which the angle rotates. To calculate the prediction step of a traditional EKF, $\mathbf{x}_{k+1|k}$, the state is represented as Equation (29).

$$\mathbf{x}_{k+1|k} = f(\mathbf{x}_k, \boldsymbol{\tau}) = \begin{bmatrix} \boldsymbol{\omega}_k + \delta t(\mathbf{I}^{-1}(\mathbf{I}\boldsymbol{\omega}_k \times \boldsymbol{\omega}_k + \boldsymbol{\tau})) \\ \mathbf{q}_k \bigotimes \begin{bmatrix} \mathbf{r}\sin(\theta/2) \\ \cos(\theta/2) \end{bmatrix} \end{bmatrix} \tag{29}$$

The symbol $\bigotimes$ represents a quaternion multiplication given in Equation (30), where $s$ is the scalar part and $\mathbf{v}$ is the vector part of the quaternion.

$$\mathbf{q}_1 \bigotimes \mathbf{q}_2 = \begin{bmatrix} s_1\mathbf{v}_2 + s_2\mathbf{v}_1 + \mathbf{v}_1 \times \mathbf{v}_2 \\ s_1 s_2 - \mathbf{v}_1 \bullet \mathbf{v}_2 \end{bmatrix} \quad \mathbf{q} = \begin{bmatrix} \mathbf{v} \\ s \end{bmatrix} \tag{30}$$

Linearization in Equation (31) uses the state error with $\phi$, the axis-angle error vector.

$$\delta\mathbf{x}_{k+1} = \mathbf{A}_k\delta\mathbf{x}_k + \mathbf{B}_k\delta\boldsymbol{\omega}_k \quad ; \delta\mathbf{x}_k = \begin{bmatrix} \boldsymbol{\omega}_k \\ \boldsymbol{\phi}_k \end{bmatrix} \tag{31}$$

The state $\mathbf{A}_k$ matrix provided in Equation (32).

$$\mathbf{A}_k = \begin{bmatrix} \mathbf{I}_{3\times3} + \delta t \begin{bmatrix} 0 & \sigma_1\omega_{k3} & \sigma_1\omega_{k2} \\ \sigma_2\omega_{k3} & 0 & \sigma_2\omega_{k1} \\ \sigma_3\omega_{k2} & \sigma_3\omega_{k1} & 0 \end{bmatrix} & \mathbf{0}_{3\times1} \\ \mathbf{I}_{4\times4}\delta t & e^{-\hat{\boldsymbol{\omega}}_k\delta t} \end{bmatrix} \tag{32}$$

The MEKF is initialized with a known state mean, $\boldsymbol{\mu}_{\mathbf{o}|\mathbf{o}}$, and covariance, $\boldsymbol{\Sigma}_{\mathbf{o}|\mathbf{o}}$, and the predict step is executed under the same formulation as the EKF in Equation (22).

Where ${}^{B}\mathbf{r}_1$ represents the first axis-angle measurement in the body frame, ${}^{N}\mathbf{r}_1$ represents the first axis-angle measurement in the normal frame, ${}^{B}\mathbf{Q}^{N}_{k+1|k}$ represents the rotation between the body frame and the normal frame for the current step, and $\mathbf{V}_k$ is the Gaussian white sensor noise, the Kalman Gain $\mathbf{K}$ is determined from Equations (33,34, 35).

$$\mathbf{z}_{k+1} = \begin{bmatrix} \boldsymbol{\omega}_{meas} \\ {}^{B}\mathbf{r}_1 \\ {}^{B}\mathbf{r}_2 \\ {}^{B}\mathbf{r}_3 \end{bmatrix} - \begin{bmatrix} \mathbf{I}_{3\times3} & 0 & 0 & 0 \\ 0 & {}^{B}\mathbf{Q}^{N}_{k+1|k} & 0 & 0 \\ 0 & 0 & {}^{B}\mathbf{Q}^{N}_{k+1|k} & 0 \\ 0 & 0 & 0 & {}^{B}\mathbf{Q}^{N}_{k+1|k} \end{bmatrix} \begin{bmatrix} \boldsymbol{\omega}_{k+1|k} \\ {}^{N}\mathbf{r}_1 \\ {}^{N}\mathbf{r}_2 \\ {}^{N}\mathbf{r}_3 \end{bmatrix} \tag{33}$$

$$\boldsymbol{C}_{k+1} = \begin{bmatrix} \mathbf{I}_{3\times3} & 0 & 0 \\ 0 & {}^{B}\hat{\mathbf{r}}_1 & 0 \\ 0 & {}^{B}\hat{\mathbf{r}}_2 & 0 \\ 0 & {}^{B}\hat{\mathbf{r}}_3 & 0 \end{bmatrix} \tag{34}$$

$$\mathbf{K}_{k+1} = \boldsymbol{\Sigma}_{k+1|k}\mathbf{C}^{T}_{k+1}(\mathbf{C}_{k+1}\boldsymbol{\Sigma}_{k+1|k}\mathbf{C}^{T}_{k+1} + \mathbf{V}_k)^{-1} \tag{35}$$

For the purposes of integration with the current simulation model, a quaternion was given as a measurement rather than axis-angle measurements. In this context, the measured quaternion was used to construct a rotation matrix of $\begin{bmatrix} {}^{R}\mathbf{r}_1 & {}^{R}\mathbf{r}_2 & {}^{R}\mathbf{r}_3 \end{bmatrix}$ that was compared to the predicted rotation matrix, ${}^{B}\mathbf{Q}^{N}_{k+1|k}$, where the the axis-angle measurements are the given basis vectors. Finally, the state estimate is updated in Equations (36, 37, 38, 39).

$$\delta\mathbf{x}_{k+1|k+1} = \mathbf{K}_{k+1}\mathbf{z}_{k+1} = \begin{bmatrix} \delta\boldsymbol{\omega}_k \\ \delta\boldsymbol{\phi}_k \end{bmatrix} \tag{36}$$

$$\mathbf{q}_{k+1|k+1} = \mathbf{q}_{k+1|k} \begin{bmatrix} \mathbf{r}\sin(\theta/2) \\ \cos(\theta/2) \end{bmatrix} \quad \theta = ||\delta\boldsymbol{\phi}_k|| \quad \mathbf{r} = \tfrac{\delta\boldsymbol{\phi}_k}{\theta} \tag{37}$$

$$\boldsymbol{\omega}_{k+1|k+1} = \boldsymbol{\omega}_{k|k} + \delta\boldsymbol{\omega}_k \tag{38}$$

$$\boldsymbol{\Sigma}_{k+1|k+1} = (\mathbf{I} - \mathbf{K}_{k+1}\mathbf{C}_{k+1})\boldsymbol{\Sigma}_{k+1|k}(\mathbf{I} - \mathbf{K}_{k+1}\mathbf{C}_{k+1})^{T} + \mathbf{K}_{k+1}\mathbf{V}_k\mathbf{K}^{T}_{k+1} \tag{39}$$

The MEKF improves upon the EKF by not making any linear assumptions about the quaternion logic. Rather than update the components of the quaternion linearly and then execute a required normalization procedure after each update step, the MEKF computes the new quaternion through a linearization around the axis of rotation. Therefore, it is still appropriate to call the MEKF a linearization of the nonlinear satellite dynamics, but its innovation comes from the treatment of the attitude quaternion.

## Unscented Kalman Filter

For applications with noisy measurements, such as determining the attitude of a spacecraft with low accuracy or high-noise attitude sensors, the UKF [11] can provide advantages over a traditional EKF or Q-MEKF [8]. The UKF manages to overcome some of the pitfalls of the EKF when estimating the nonlinearities in the dynamics model due to large uncertainties. It is able to accomplish this by implementing weighted sigma points to calculate more accurate mean and covariance estimates. These weighted sigma points are calculated using an unscented transformation, which converts the mean, covariance, and dimensions of the state vector into the weighted sigma points needed to implement the UKF [6].

In the UKF, the weighted sigma points are found using the unscented transform in Equation (40).

$$(\mathbf{x}^i_{t-1|t-1}, w^i_{t-1|t-1}) = UT(\boldsymbol{\mu}_{t-1|t-1}, \boldsymbol{\Sigma}_{t-1|t-1}) \tag{40}$$

The predict step of the UKF is represented as Equations (41, 42, 43).

$$\bar{\mathbf{x}}^i_{t|t-1} = \mathbf{f}(\mathbf{x}^i_{t-1|t-1}, \mathbf{u}_{t-1}) \tag{41}$$

$$(\boldsymbol{\mu}_{t|t-1}, \bar{\boldsymbol{\Sigma}}_{t|t-1}) = UT^{-1}(\bar{\mathbf{x}}^i_{t|t-1}, w_{t-1|t-1}) \tag{42}$$

$$\boldsymbol{\Sigma}_{t|t-1} = \bar{\boldsymbol{\Sigma}}_{t|t-1} + \mathbf{Q}_t \tag{43}$$

The update step of the UKF is represented as Equations (44, 45, 46).

$$(\mathbf{x}^i_{t|t-1}, w^i_{t|t-1}) = UT(\boldsymbol{\mu}_{t|t-1}, \boldsymbol{\Sigma}_{t|t-1}) \tag{44}$$

$$\mathbf{y}^i_{t|t-1} = \mathbf{g}(\mathbf{x}^i_{t|t-1}, \mathbf{u}_t) \tag{45}$$

$$\hat{\mathbf{y}}_{t|t-1} = \sum_{i=0}^{n} w^i \mathbf{y}^i_{t|t-1} \tag{46}$$

The Gaussian Estimation equations are applied as Equations (47, 48, 49, 50).

$$\boldsymbol{\mu}_{t|t} = \boldsymbol{\mu}_{t|t-1} + \boldsymbol{\Sigma}^{XY}_{t|t-1}(\boldsymbol{\Sigma}^{Y}_{t|t-1})^{-1}(\mathbf{y}_t - \hat{\mathbf{y}}_{t|t-1}) \tag{47}$$

$$\boldsymbol{\Sigma}_{t|t} = \boldsymbol{\Sigma}_{t|t-1} - \boldsymbol{\Sigma}^{XY}_{t|t-1}(\boldsymbol{\Sigma}^{Y}_{t|t-1})^{-1}(\boldsymbol{\Sigma}^{XY}_{t|t-1})^T \tag{48}$$

where

$$\boldsymbol{\Sigma}^{Y}_{t|t-1} = \sum_{i=0}^{2n} w^i(\mathbf{y}^i_{t|t-1} - \hat{\mathbf{y}}_{t|t-1})(\mathbf{y}^i_{t|t-1} - \hat{\mathbf{y}}_{t|t-1})^T + \mathbf{R}_t \tag{49}$$

and

$$\boldsymbol{\Sigma}^{XY}_{t|t-1} = \sum_{i=0}^{2n} w^i(\mathbf{x}^i_{t|t-1} - \boldsymbol{\mu}_{t|t-1})(\mathbf{y}^i_{t|t-1} - \hat{\mathbf{y}}_{t|t-1})^T \tag{50}$$

# Results

The three types of filters described above were applied to a satellite system modeled on the TESS spacecraft. Table 1 shows the relevant satellite parameters used in the simulation.

| Satellite Parameter | Value |
|---|---|
| $I_x(kg \cdot m^2)$ | 197.22 |
| $I_y(kg \cdot m^2)$ | 222.835 |
| $I_z(kg \cdot m^2)$ | 277.6 |
| $\sigma_{Process,\boldsymbol{\omega}}$ | $10^{-6}$ |
| $\sigma_{Process,\boldsymbol{q}}$ | $10^{-6}$ |
| $\sigma_{Sensor,\boldsymbol{\omega}}$ | $10^{-4}$ |
| $\sigma_{Sensor,\boldsymbol{q}}$ | $10^{-4}$ |

Table 1: Satellite parameters

Three different trials were explored for this project. First, a benchmark trial was conducted at relatively low initial rotation rates and high frequency of measurement. Second, a trial was conducted at much higher initial rotation rates while maintaining high frequency of measurement to test filter performance when the system is more nonlinear. Since the degree of nonlinearity scales with the rate of rotation, larger rotation rates describe more nonlinear systems. The UKF was expected to perform significantly better in the presence of high rotation rates since system dynamics are linearized within the EKF and MEKF. The third trial explored a slow rotation rate and low frequency of measurement. In instances where the attitude measurement is only available intermittently, the choice of filter becomes much more important in modeling true dynamics. Different attitude sensors may deliver measurements at a low frequency, invalidating the linearization of dynamics within the EKF and MEKF. Additionally, the frequency of filtering may be constrained by the computational power of the satellite; filtering presents a significant burden on the satellite CPU. The UKF was also expected to outperform the EKF and MEKF with a slower measurement frequency. Since the process noise value did not change when the time step shifted, the relative process noise on the system decreased, although the sensor noise remained the same. Table (2) summarizes the attributes of these trials.

| Attribute | Trial 1 | Trial 2 | Trial 3 |
|---|---|---|---|
| Rotation Rate (deg/s) | 2 x 4 x 8 | 30 x 30 x 30 | 4 x 4 x 4 |
| $\Delta t$ (s) | 0.001 | 0.001 | 0.05 |
| Initial Quaternion | $[1\ 0\ 0\ 0]^T$ | $[1\ 0\ 0\ 0]^T$ | $[0\ 0\ 0\ 1]^T$ |

Table 2: Trial attributes

## Trial 1

For the benchmark trial, all three filters provided comparable state estimates as shown in Figure 3. The UKF performed poorly for the quaternion relative to the EKF and MEKF, however for estimating rotation rates it marked significant improvement over the EKF and MEKF as shown in Table 3. Since the time step for this simulation was very small, the MEKF demonstrated marginal improvement over the EKF state estimate.

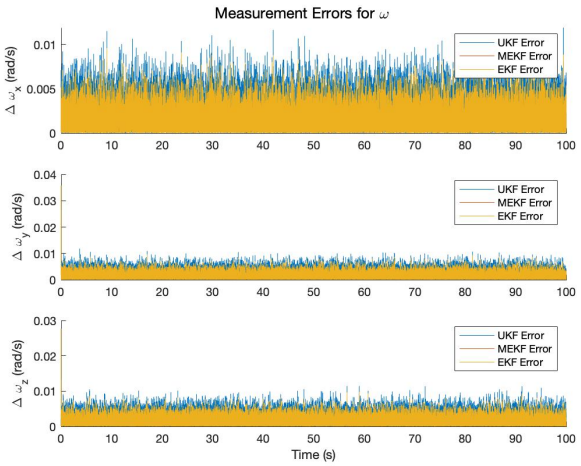


(a) Trial 1 - Rotation Rate

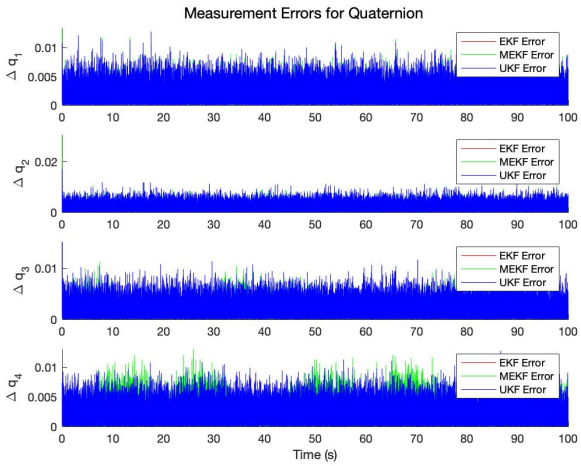


(b) Trial 1 - Quaternion

Figure 3: Results of UKF, MEKF, and EKF state estimation for Trial 1.

| | EKF | MEKF | UKF |
|---|---|---|---|
| Angular Velocity $(\frac{degrees}{s})$ | 0.697 | 0.697 | 0.017 |
| Quaternion | 0.143 | 0.161 | 0.167 |

Table 3: Trial 1 RMS errors after 100 seconds

## Trial 2

With more nonlinear system dynamics in trial 2, the UKF demonstrated better performance over both the EKF and MEKF as shown in Figure 4. The increase in rotation rate mainly disturbed the linearization of the rotation rate in the Euler rigid body dynamics, so the quaternion innovation of the MEKF provided no additional benefit. The rotation rate errors of the MEKF and EKF were seen to perform identically, while the UKF performed well in the presence of large rotation rates as shown in Table 4.

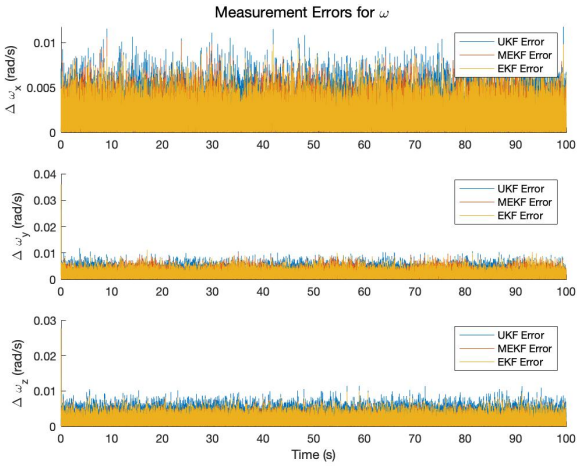


(a) Trial 2 - Rotation Rate

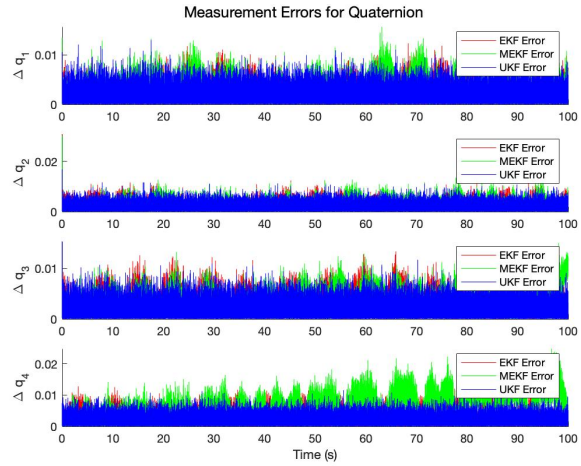


(b) Trial 2 - Quaternion

Figure 4: Results of UKF, MEKF, and EKF state estimation for Trial 2.

| | EKF | MEKF | UKF |
|---|---|---|---|
| Angular Velocity ($\frac{degrees}{s}$) | 7.420 | 7.420 | 0.017 |
| Quaternion | 0.217 | 0.306 | 0.168 |

Table 4: Trial 2 RMS errors after 100 seconds

## Trial 3

When the frequency of measurement was decreased by a factor of 20, the UKF significantly outperformed the EKF and UKF in both attitude and rotation rate as shown in Figure 5. Since the process noise value for the system was unaltered while the frequency of the filter was decreased, the comparable process noise to the system was decreased, allowing the UKF to perform better in Trial 3 than in Trials 1 and 2. The innovation of the quaternion update that distinguishes the MEKF allowed this method to deliver more accurate attitude and rotation rate estimates. The attitude improvements are due to the method of determining the next quaternion in the update step of the MEKF through quaternion logic, where the EKF simply normalizes a linearized quaternion update. The improvement on the rotation rate estimate is due to a cascading effect from the improvement on the attitude delivered through the MEKF.

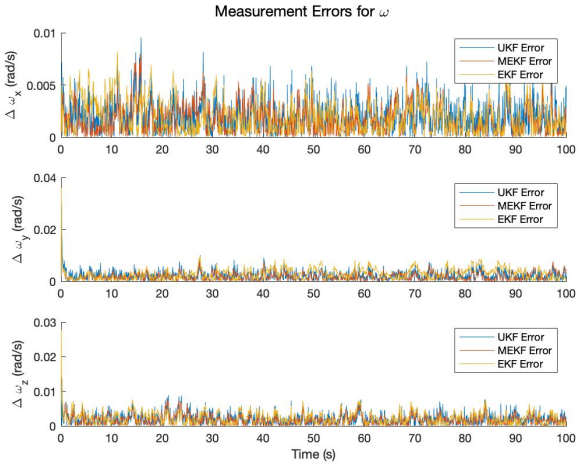


(a) Trial 3 - Rotation Rate

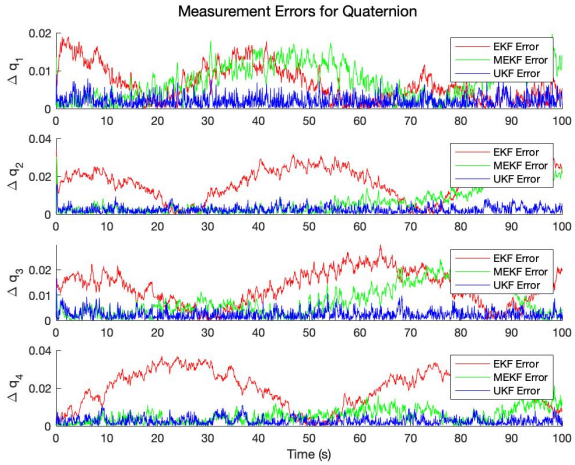


(b) Trial 3 - Quaternion

Figure 5: Results of UKF, MEKF, and EKF state estimation for Trial 3.

| | EKF | MEKF | UKF |
|---|---|---|---|
| Angular Velocity ($\frac{degrees}{s}$) | 1.324 | 1.037 | 0.017 |
| Quaternion | 0.149 | 0.078 | 0.027 |

Table 5: Trial 3 RMS errors after 100 seconds

Overall, the three trials demonstrated the relative accuracy of the UKF over the EKF and MEKF, especially in the presence of high rotation rate or low filter frequency. These results suggest the validity of implementing a UKF in satellite systems undergoing off-nominal functionality or that are subjected to more extreme operations, such as systems that are expected to slew rapidly.

The EKF and MEKF demonstrated periodic behavior in their errors in Figure 5 due to the representation of the quaternion error as $q_{error} = q_{truth} - q_{estimated}$. When one quaternion element peaks in error, the

other elements are similarly decreased. When the quaternion errors are represented as angle errors based on a conversion between the quaternion and an axis angle representation, these periodic errors disappear.

One important aspect of Kalman Filtering is the amount of computational cost and processing time that is required for filter implementation. On average, the UKF took between 1.5 to 2 times as long to implement compared to the EKF or MEKF estimates as shown in Table 6. This presents a potentially severe boundary to implementation, especially for processing-constrained systems. Though a UKF may out-perform other methods for low filtering frequencies, it may be more efficient to increase the filter frequency and continue to use either an EKF or MEKF. The primary benefactors of the UKF are satellites with excess processing power that may expect extreme operation conditions.

| Method | Time (seconds) |
|---|---|
| EKF | 5.567 |
| MEKF | 17.50 |
| UKF | 34.99 |

Table 6: Total computation time for each filter

# Conclusions and Future Work

In this paper we explored the implementation of state estimators to derive true dynamics of a spacecraft from noisy measurements. The full spacecraft dynamics were modeled without internal gyroscopes using the Euler equations and quaternions. An inertial tensor based on the TESS spacecraft was diagonalized using the eigenvalues of the original matrix. The spacecraft's attitude was then simulated over time with noise in both the process and the measurement. Three different filters were applied to the measured attitude: an Extended Kalman Filter (EKF), a Multiplicative Extended Kalman Filter (MEKF), and an Unscented Kalman Filter. For the EKF and MEKF, the dynamics of the satellite was linearized according to the normal process.

For normal spacecraft operations with low rotation rates and high frequencies of measurement, the three filters were almost interchangeable in their accuracy. With more nonlinear dynamics, the EKF and MEKF showed periodic errors and significant inaccuracies when compared to the UKF. Additionally, the UKF demonstrated significant improvement over the EKF and MEKF when the frequency of measurement was decreased.

The results of this study reaffirm the ability of the EKF to predict the attitude of a spacecraft given small rotation rates and frequent attitude measurements. For the purposes of optical intersatellite links, fast and accurate slewing is required for constellation operation that invalidates the EKF. As satellites become smaller, more efficient, and cheaper, the frequency of measurement may need to be decreased in order to cede computational power to other satellite processes. Although the UKF requires more computational investment by the satellite processor, the required frequency of observation drops substantially.

Future work includes varying the processing capabilities of spacecraft and comparing filter performance, as this project stopped short of investigating processing requirements of the different filters. To further validate the UKF for nonlinear small satellite slew maneuvers, the algorithm should be implemented on flight hardware and given an adequate duty cycle to ensure that satellite operations competing for computation power can still be guaranteed. Additionally, the moments of inertia used in this project were relatively similar. Future satellites, such as spacecraft in the Starlink constellation, have demonstrated new form factors that may inhibit application of the EKF or MEKF to linearized dynamics.

# References


[1] Markley F. Crassidis, John and Yang Cheng. Survey of Nonlinear Attitude Estimation Methods. *Proceedings of the IEEE 2000 Adaptive Systems for Signal Processing, Communications, and Control Symposium*, 10 2000.

[2] Yifan Deng, Zhigang Wang, and Lei Liu. Unscented Kalman Filter for Spacecraft Pose Estimation Using Twistors. *Journal of Guidance, Control, and Dynamics*, 39:1844–1856, 08 2016.

[3] Farhan A. Faruqi and Kenneth J. Turner. Extended Kalman Filter Synthesis for Integrated Global Positioning/Inertial Navigation Systems. *Applied Mathematics and Computation*, pages 213–227, 10 2000.

[4] Nuno Filipe, Michail Kontitsis, and Panagiotis Tsiotras. Extended Kalman Filter for Spacecraft Pose Estimation Using Dual Quaternions. *Journal of Guidance, Control, and Dynamics*, 38:1625–1641, 09 2015. doi: 10.2514/1.G000977.

[5] S. Janson and R. Welle. The NASA optical communication and sensor demonstration program. *Proceedings of the 27th Annual AIAA/USU Conference on Small Satellites*, 08 2013.

[6] S.J. Julier and J.K. Uhlmann. New Extension of the Kalman Filter to Nonlinear Systems. *Signal Processing, Sensor Fusion, and Target Recognition VI*, 3068:182–194, 1997. doi: doi:10.1117/12.280797.

[7] E.J. Lefferts, F.L. Markley, and M.D. Shuster. Kalman Filtering for Spacecraft Attitude Estimation. *Journal of Guidance, Control, and Dynamics*, 5:417–429, 10 1982.

[8] Guang-Fu Ma and Xue-Yuan Jiang. Unscented Kalman Filter for Spacecraft Attitude Estimation and Calibration Using Magnetometer Measurements. *2005 International Conference on Machine Learning and Cybernetics*, 1:506–511, 2005.

[9] E. Perez, M. Bailly, and J.M. Pairot. Pointing Acquisition And Tracking System For Silex Inter Satellite Optical Link. *Proceedings of SPIE, Acquisition, Tracking, and Pointing III*, 1111, 09 1989.

[10] Toni Tolker-Nielsen and Gotthard Oppenhauser. In-Orbit Test Result of an Operational Optical Intersatellite Link Between ARTEMIS and SPOT4, SILEX. *Proceedings SPIE, Free-Space Laser Communication Technologies XIV*, 4635, 4 2002.

[11] Eric A. Wan and Rudolph van der Menve. The Unscented Kalman Filter for Nonlinear Estimation. *Proceedings of the IEEE 2000 Adaptive Systems for Signal Processing, Communications, and Control Symposium*, 10 2000.